Check for updates

The rational design of hierarchical MoS$_2$ nanosheet hollow spheres sandwiched between carbon and TiO$_2$@graphite as an improved anode for lithium-ion batteries†

Faze Wang, [ID] [abc] Fanggang Li,[a] Maojun Zheng, [ID] *[a] Yanbo Li*[b] and Li Ma[d]

Molybdenum disulfide (MoS$_2$) shows high capacity but suffers from poor rate capability and rapid capacity decay, which greatly limit its practical applications in lithium-ion batteries. Herein, we successfully prepared MoS$_2$ nanosheet hollow spheres encapsulated into carbon and titanium dioxide@graphite, denoted as TiO$_2$@G@MoS$_2$@C, *via* hydrothermal and polymerization approaches. In this hierarchical architecture, the MoS$_2$ hollow sphere was sandwiched by graphite and an amorphous carbon shell; thus, TiO$_2$@G@MoS$_2$@C exhibited effectively enhanced electrical conductivity and withstood the volume changes; moreover, the aggregation and diffusion of the MoS$_2$ nanosheets were restricted; this advanced TiO$_2$@G@MoS$_2$@C fully combined the advantages of a three-dimensional architecture, hollow structure, carbon coating, and a mechanically robust TiO$_2$@graphite support, achieving improved specific capacity and long-term cycling stability. In addition, it exhibited the high reversible specific capacity of 823 mA h g^{-1} at the current density of 0.1 A g^{-1} after 100 cycles, retaining almost 88% of the initial reversible capacity with the high coulombic efficiency of 99%.

Introduction

Lithium-ion batteries (LIBs) have attracted extensive attention as potential power sources for significant application in electric vehicles because of their long cycle life and high power density.[1–3] Currently, graphite is predominantly used as an anode material for commercial LIBs. However, due to the relatively low theoretical capacity of graphite (around 372 mA h g^{-1}), the commercial LIBs cannot meet the energy storage requirements for large-scale electric vehicles in the future.[4,5] Thus, it is highly desirable to exploit alternative anode materials with higher capacity and excellent cycling stability. Transition metal oxides and sulfides as promising anode materials have shown striking electrochemical performance in LIBs.[6–8] Among these alternatives, a two-dimensional (2D) layered material, molybdenum disulfide (MoS$_2$), has received

significant attention due to its open framework facilitating the insertion of Li$^+$ reversibly; this leads to high reversible capacity.[9–11] However, bare MoS$_2$ electrodes exhibit poor rate capability and fast capacity fading caused by low conductivity, huge volume variation and aggregation during cycling.[12–16] In addition to MoS$_2$, TiO$_2$ is considered as one of the most potential alternative anode materials owing to its excellent cycling stability, low cost and environmental friendliness. Several MoS$_2$/TiO$_2$ composites have been reported with improved electrochemical performance owing to their synergistic effects.[17–25] When TiO$_2$ and MoS$_2$ are combined in a smart system, TiO$_2$ with excellent chemical stability and low volume variation (<4%) is obtained,[26] acting as a skeleton to effectively accommodate the strain of volume changes. Moreover, the high capacity of MoS$_2$ can compensate the low specific capacity of TiO$_2$. However, the MoS$_2$ sheets present on the surface of TiO$_2$ are still prone to strong restacking, and the intermediate polysulfides dissolve during repeated charge/discharge processes.[27,28] Thus, the rational design of advanced hybrid materials of MoS$_2$ and other functional components with complementary electrochemical properties is significantly desired to overcome these inherent obstacles.

To date, significant efforts have been made to integrate MoS$_2$ with carbonaceous materials (such as graphene, carbon nanotubes, amorphous carbon, carbon nanosheets, *etc.*),[14,29–44] and all these composites exhibit better electrochemical performances as anode materials for LIBs due to the fully synergistic

[a]*Key Laboratory of Artificial Structure and Quantum Control, Ministry of Education, Department of Physics and Astronomy, Shanghai Jiao Tong University, Shanghai, 200240, China. E-mail: mjzheng@sjtu.edu.cn*

[b]*Institute of Fundamental and Frontier Sciences, University of Electronic Science and Technology of China, Chengdu, 610054, China. E-mail: yanboli@uestc.edu.cn*

[c]*Walter Schottky Institut, Physik Department, Technische Universität München, Garching 85748, Germany*

[d]*School of Chemistry and Chemical Technology, Shanghai Jiao Tong University, Shanghai, 200240, China*

† Electronic supplementary information (ESI) available. See DOI: 10.1039/c9na00019d

effect of nanostructured MoS_2 and superior conductivity of highly flexible carbon materials. The carbon component could effectively accommodate the strain of volume change during cycling, prevent the aggregation and improve the electric conductivity.[45,46] Despite the abovementioned success, there are still obstacles that hinder the further development of MoS_2 because of the polysulfide shuttling effect causing capacity loss due to the lack of a top conductive protection layer. Therefore, it is highly required to develop an ideal hierarchical architecture with enhanced electrical conductivity and better electrode stability in which the synergistic effects of every component are manifested.

Herein, we designed template-assisted fabrication of hierarchical MoS_2 nanosheet hollow spheres sandwiched between a graphite-coated TiO_2 core and an amorphous carbon shell. Compared with the case of the simple core–shell $TiO_2@MoS_2$ nanostructure, the introduction of a graphite inter-layer and a carbon shell has two advantages: on the one hand, graphitic coating the mesoporous TiO_2 hollow spheres provided a rapid pathway for lithium and electron transfer between the abundant interfaces of the sandwich-like $MoS_2/G/TiO_2$, accommodated the volume change and maintained the integrity of the hollow structure; on the other hand, the deposited carbon coating on the surface of the MoS_2 nanosheets could prevent MoS_2 from aggregation and the diffusion of sulfur while improving the electron conductivity and modifying the interface between the electrode/electrolyte. The synergistic effect of these three components and the hierarchical nanostructure endowed the carbon-coated $TiO_2@G@MoS_2$ hollow sphere with improved electrochemical properties for application in LIBs.

Results and discussion

The overall synthesis procedure of the triple-layer $TiO_2@G@MoS_2$ hollow nanosphere is illustrated in Fig. 1a, which involves four steps. First, SiO_2 nanospheres were prefabricated as a core template based on the Stöber method.[47] Fig. 1b shows the scanning electron microscopy (SEM) image of the SiO_2 nanosphere with the diameter of ca. 290 nm, and the spheres are significantly monodisperse, smooth and uniform. In the second step, amorphous TiO_2 shells were deposited on the SiO_2 nanospheres via a versatile kinetics-controlled coating method. Then, the as-prepared $SiO_2@TiO_2$ spheres were placed in a glucose solution and hydrothermally treated. In this step, the surface of the mesoporous TiO_2 network was covered with decomposed glucose. Due to the catalytic effect of TiO_2 nanoparticles, the glucose-coated $SiO_2@TiO_2$ spheres were transformed into $SiO_2@TiO_2@$graphitic carbon ($SiO_2@TiO_2@G$) core–shell nanospheres via calcination at 800 °C for 5 hours. The SEM images of the $SiO_2@TiO_2@G$ samples show larger monodisperse spheres with the uniform diameter of 500 nm (Fig. 1c). The high-magnification SEM image clearly revealed that the surface consisted of primary small nanoparticles. Finally, the vertically oriented MoS_2 nanosheets grew on the surface of $SiO_2@TiO_2@G$ by an L-cysteine-assisted hydrothermal method. During the hydrothermal process, the MoO_4^{2-} anions were reduced to MoS_2 by S^{2-} released from L-cysteine. Moreover, multifunctional groups (SH, NH_2, and COO) of L-cysteine could guide the self-assembly growth of the MoS_2 nanosheets on the surface of the carbon intermediate layer.[29] The sample was further treated at 500 °C for 2 hours under a vacuum condition to obtain highly crystalline MoS_2. Fig. 1d shows the typical SEM images of the as-synthesized $SiO_2@TiO_2@G@MoS_2$ nanosphere structures, which indicates that the $SiO_2@TiO_2@G$ spheres are uniformly coated with the MoS_2 shell, and the diameter of these multi-layer core–shell spheres increases to ca. 600 nm. The high-magnification images revealed that the MoS_2 shell was composed of interconnected vertically oriented ultrathin nanosheets. After the selective removal of SiO_2 template by HF immersion, triple-layer $TiO_2@G@MoS_2$ hollow nanospheres were obtained (Fig. 1e).

As shown in Fig. 2a, the interior space is revealed from an incomplete hollow sphere. The FESEM image of partly peeled $TiO_2@G@MoS_2$ hollow nanospheres clearly discloses that the hierarchical nanospheres consist of a mesoporous TiO_2 core and a MoS_2 nanosheet shell (Fig. 2b). The detailed core–shell hollow structure was further characterized by a transmission electron microscope (TEM). From a single core–shell nanosphere, it can be observed that the MoS_2 nanosheet shell was uniformly attached to the surface of TiO_2 (Fig. 2c). All the hollow
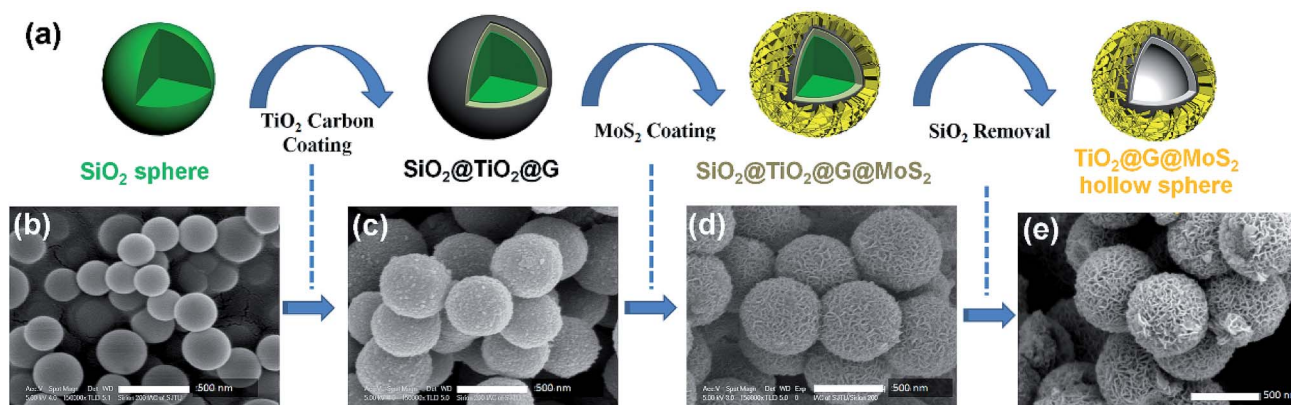

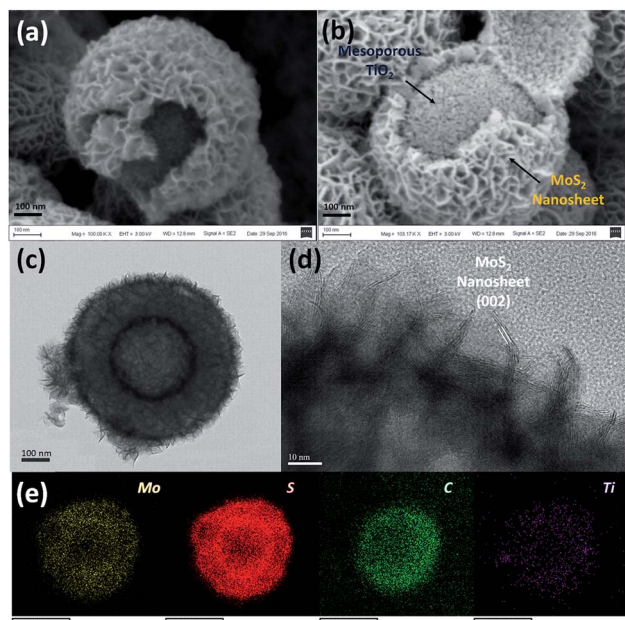**Fig. 1** (a–e) Schematic of the synthesis of hierarchical $TiO_2@G@MoS_2$ hollow nanospheres.

Fig. 2 (a and b) SEM, (c) TEM and (d) HRTEM images of the TiO_2@-G@MoS_2 hollow nanospheres. (e) EDX-elemental mapping images of Mo, S, C and Ti.

spheres showed the uniform shell thickness of about 150 nm and an inner cavity of ~300 nm, which was consistent with the diameter of the SiO_2 templates. The HRTEM images show the lattice fringes of the MoS_2 nanosheet structures. The thickness of the nanosheets was about several nanometers. The distance of the parallel lattice planes at the edge of the MoS_2 nanosheet was about 6.5 Å, which corresponded to the d spacing of the (002) planes of MoS_2 (Fig. 2d). To investigate the element distribution of MoS_2, carbon and TiO_2 in the TiO_2@G@MoS_2 hollow nanospheres, energy dispersive X-ray (EDX) spectroscopy was carried out (Fig. 2e). The elemental mapping images show that the Mo and S elements formed the shell and the core consisted of C and Ti with smaller diameter. These results directly demonstrated the hierarchical surface modification of the MoS_2 nanosheet on graphite-coated TiO_2 hollow spheres.

The XRD patterns (Fig. 3a) were acquired for the TiO_2@-G@MoS_2 hollow nanospheres to obtain their crystallographic

structure information. The diffraction peaks at $2\theta = 14.3$, 32.5, 36.0 and 58.5 correspond to the (002), (100), (102) and (110) planes of 2H–MoS_2 (JCPDS no. 37-1492).[48] In addition, the characteristic diffraction peaks assigned to (101), (200), (105), (111) and (204) of hexagonal TiO_2 (JCPDS no. 21-1272) were present. Further insight into the nanostructure of TiO_2@G@MoS_2 was achieved by examination of its Raman spectrum (Fig. 3b). The characteristic Raman shifts at about 377 and 400 cm^{-1} expected for the E_{2g}^1 and A_{1g} vibrational modes of hexagonal MoS_2 were clearly observed.[49] Moreover, the presence of the TiO_2 core was confirmed by the Raman peaks emerging at 150, 282, 333 and 639 cm^{-1}, which corresponded to the vibrational modes of the Ti–O bonds.[50] The bands at 1357 and 1580 cm^{-1} were the typical D and G lines of graphitic carbon.[51] Note that two strong bands emerging at 817 and 990 cm^{-1} can be assigned to SiC. In the annealing process, we predicted that the amorphous carbon would evaporate into the mesoporous TiO_2 shell under a high vacuum condition; this would induce the formation of SiC. The existence of SiC would be beneficial for the improvement of stability because of its high mechanical strength.

X-ray photoelectron spectroscopy (XPS) was employed to characterize the chemical nature and bonding state of the TiO_2@G@MoS_2 hollow spheres. Fig. 4a displays the detailed XPS scans of the Mo, S and Ti binding energies. All the spectra were calibrated by a carbon 1s peak located at 284.50 eV. Moreover, two peaks at 229.3 and 228.4 eV were assigned to Mo 3d5/2 and Mo 3d3/2, respectively (Fig. 4b).[33,52,53] Fig. 4c shows the XPS spectrum of the S 2p region. In the high-resolution spectrum of Ti 2p (Fig. 4d), two peaks at 464.5 and 458.8 eV were attributed to Ti 2p1/2 and Ti 2p3/2, respectively. However, the Ti 2p peaks were relatively weak, indicating the full coverage of the MoS_2 shell. The XPS results further confirmed the coexistence of MoS_2 and TiO_2 in the TiO_2@G@MoS_2 hierarchical structure, which agreed well with the XRD and Raman results.

The electrochemical performance of the TiO_2@G@MoS_2 hollow structures as lithium-ion battery anodes was examined by assembling them into Li half-cells. Electrodes made up of the pure TiO_2 hollow spheres and MoS_2 nanoparticles were also prepared for comparison. Fig. 5a shows the cyclic voltammograms (CVs) of the initial three discharge/charge cycles at the scan rate of 0.1 mV s^{-1} within the potential window of 0.0–3.0 V (*versus* Li^+/Li). In the first cycle, the two irreversible peaks at
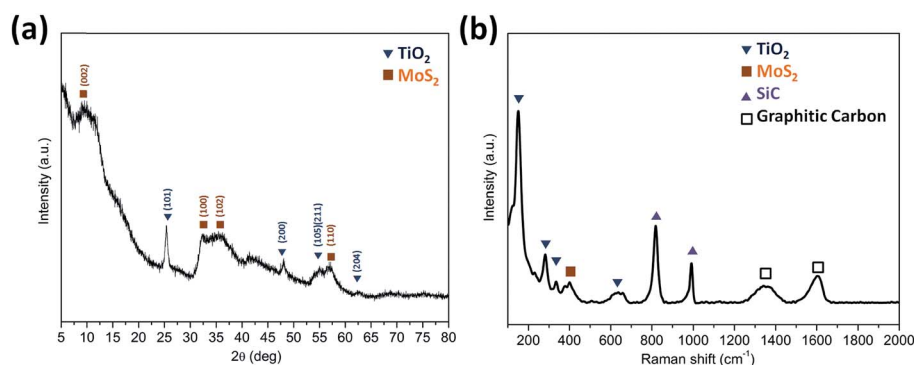

Fig. 3 (a) An XRD pattern and (b) the Raman spectrum of the TiO_2@G@MoS_2 hollow nanosphere.

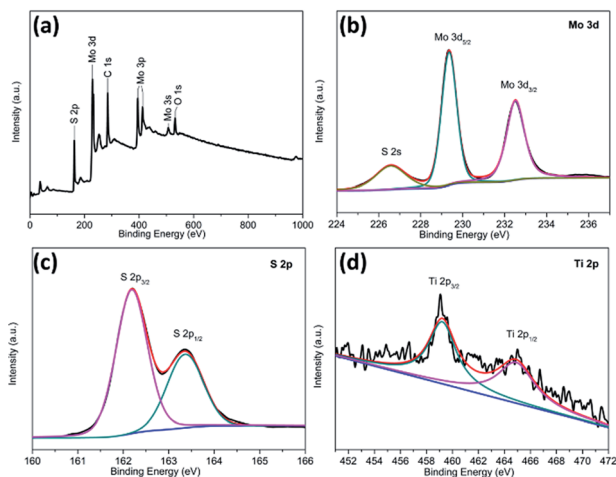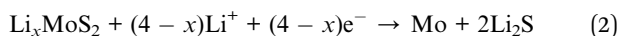**Fig. 4** XPS spectra for the TiO$_2$@G@MoS$_2$ hollow nanospheres: (a) the survey spectrum and high-resolution (b) Mo 3d, (c) S 2p, and (d) Ti 2p spectra.

1.127 and 0.473 correspond to the phase transition of MoS$_2$, resulting from the intercalation of Li$^+$ ions and the decomposition of MoS$_2$ into Mo NPs, respectively.[54–57]

$$MoS_2 + xLi^+ + xe^- \rightarrow Li_xMoS_2 \quad (1)$$

$$Li_xMoS_2 + (4 - x)Li^+ + (4 - x)e^- \rightarrow Mo + 2Li_2S \quad (2)$$

These peaks disappeared in the second and third discharge processes because few amorphous MoS$_2$ lattices were reformed

after the first charge process (lithium extraction). After the first cycle, the electrode was mainly composed of Mo and S instead of initial MoS$_2$.[33] In the successive second and third discharge processes, a new broad peak appeared at 1.917 V, corresponding to the presence of a multistep lithium insertion mechanism, which involved the lithiation of TiO$_2$ and S to form Li$_x$TiO$_2$ and Li$_2$S, respectively.[29,58]

$$S + 2Li^+ + 2e^- \leftrightarrow LiS_2 \quad (3)$$

$$TiO_2 + xLi^+ + xe^- \leftrightarrow Li_xTiO_2 \quad (4)$$
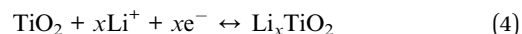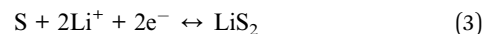
In the charging process, there was an oxidation peak at 2.37 V with few changes in the subsequent sweeps, corresponding to the lithium extraction process.[30,59] Moreover, a broad peak at 1.75 V could be attributed to the partial oxidation of Mo to Mo^{4+}.[56] These results illustrate that both MoS$_2$ and TiO$_2$ made a contribution to the charge–discharge capacity.

Fig. 5b shows the discharge–charge potential profiles of the TiO$_2$@G@MoS$_2$ hollow spheres in the 1st, 2nd and 3rd cycle at the current density of 0.1 A g^{-1} between 0.01 V and 3 V. In agreement with the CV results, two potential plateaus at 1.12 V and 0.47 V were observed in the first discharge process, which respectively corresponded to the phase transition of MoS$_2$ and the conversion reaction process. In the subsequent discharge curves, the plateaus obtained in the first discharge disappeared, whereas a new plateau appeared at 1.8 V, which was attributed to a multi-step lithium insertion process. During the charging process, a conspicuous potential plateau at about 2.3 V was observed, which was also in accordance with the CV study.
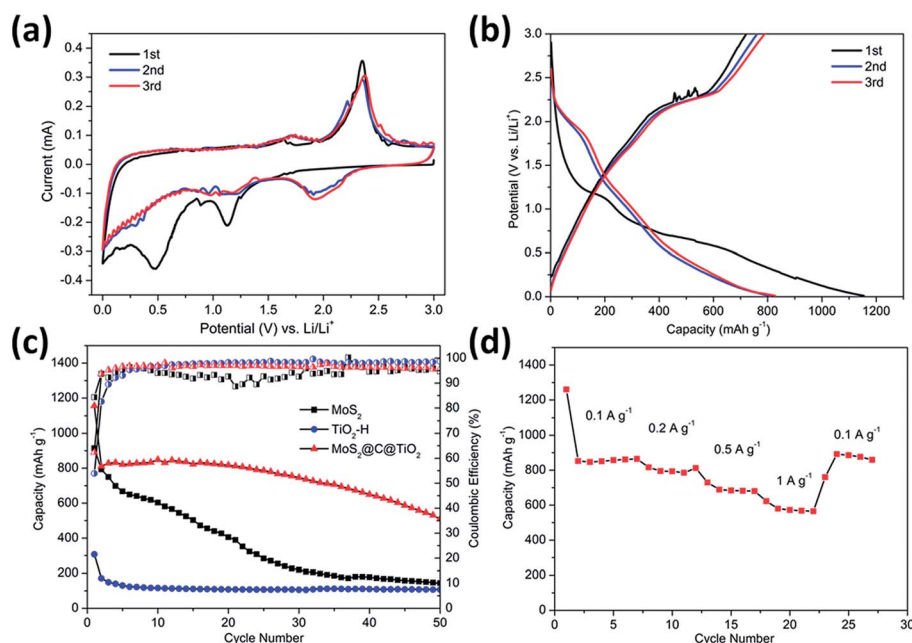

Fig. 5 (a) Cyclic voltammetry curves of the TiO$_2$@G@MoS$_2$ hollow nanospheres at the scan rate of 0.5 mV s^{-1} in the voltage range of 0.01–3 V (vs. Li/Li$^+$). (b) Charge–discharge voltage profiles at the current density of 0.1 A g^{-1} of the TiO$_2$@G@MoS$_2$ hollow nanospheres. (c) Comparative cycling performance of the pure MoS$_2$ particle, TiO$_2$ hollow sphere and TiO$_2$@G@MoS$_2$ hollow sphere electrodes, and the corresponding coulombic efficiency. (d) Rate capability of the TiO$_2$@G@MoS$_2$ electrode.

The cycling performances of the TiO_2@G@MoS_2 hollow spheres as well as pure MoS_2 and TiO_2 hollow spheres were evaluated at the discharge current density of 0.1 A g^{-1}, as shown in Fig. 5c. MoS_2 delivered capacity fading from 914 mA h g^{-1} at the initial cycle to 143 mA h g^{-1} at the 50th cycle during discharge/charge cycles due to aggregation and pulverization. Moreover, the TiO_2 hollow spheres exhibited excellent cycling stability; however, the capacity was only 105 mA h g^{-1} after 50 cycles. The lower charge capacities were mainly attributed to the lower theoretical capacity of TiO_2. In contrast, the hierarchical hollow spheres showed significantly enhanced capacity and cycling stability. The initial discharge and charge specific capacities were 1330 and 908 mA h g^{-1}, respectively, leading to the coulombic efficiency (CE) of 62%, which quickly stabilized at approximately 96% from the second cycle, being close to the coulombic efficiency of the TiO_2 hollow spheres. Compared to the case of the MoS_2 particles, the increased coulombic efficiency of the TiO_2@G@MoS_2 spheres was mainly attributed to their hollow structure since the hollow sphere architecture could provide large surface area and shorten the lithium ion diffusion path; moreover, the TiO_2@G@MoS_2 electrodes displayed an extraordinary capacity of 860 mA h g^{-1} in the first 20 cycles, which significantly exceeded that of either individual components. We suggest that the high theoretical capacity of the MoS_2 shell, the superior cycling stability performance of the TiO_2 hollow core and the excellent electric conductivity of the graphitic carbon interlayer are synergistically combined in the hierarchical TiO_2@G@MoS_2 composite electrode. Fig. 5d shows the rate capacity of triple-layer TiO_2@G@MoS_2 hollow sphere electrode at various current densities ranging from 0.1 to 1 A g^{-1}. The specific discharge capacities of the composite were about 860, 780, 680, and 570 mA h g^{-1} upon cycling at 0.1, 0.2, 0.5, and 1 A g^{-1}, respectively. When back to 0.1 A g^{-1}, the capacity returned to 860 mA h g^{-1}, indicating good rate performance of the TiO_2@G@MoS_2 composite.

However, upon long-term discharge/charge processes, the cycling performance of the TiO_2@G@MoS_2 electrodes was still poor owing to the aggregation and pulverization of the MoS_2 nanosheet shell, which contributed to most of the capacity as well as the highly conductive laminated layers to offer high interfacial contact areas and shorten the lithium ion diffusion paths.[60,61] Therefore, the carbon thin shell was chosen as the top conductive protective layer to alleviate the volume changes, prevent the aggregation and pulverization of MoS_2 and enhance the overall electronic conductivity of the electrode.[62] The resorcinol–formaldehyde resin polymer shell was first deposited on the TiO_2@G@MoS_2 sphere. After carbonization of the polymer shell precursors under an ultrahigh vacuum at 600 °C for 2 hours, the core–shell carbon-coated TiO_2@G@MoS_2 hollow sphere electrode was obtained. It was observed that the nanospheres retained their spherical shape; moreover, after coating, their surface became smooth (instead of showing vertically orientated MoS_2 nanosheets); this confirmed the uniform carbon coating (Fig. 6a and b). The TEM images demonstrate that the multiple-layer carbon coating TiO_2@G@MoS_2 sphere shows a similar hollow structure as TiO_2@G@MoS_2, but with a thin carbon shell coated on the surface of
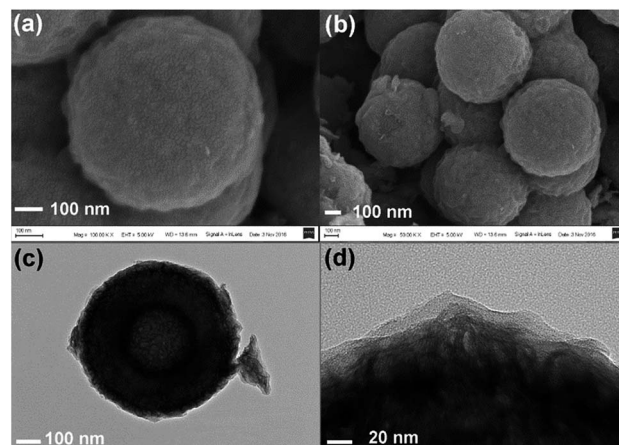

Fig. 6 (a and b) SEM, (c) TEM and (d) HRTEM images of carbon-coated TiO_2@G@MoS_2 hollow nanosphere.

MoS_2 (Fig. 6c). The curved MoS_2 nanosheets were encapsulated into an amorphous carbon layer with a thickness of 20 nm (Fig. 6d). To determine the pore structure and surface area of the as-prepared TiO_2@G@MoS_2@C, the N_2 adsorption/desorption test was conducted, as shown in Fig. S1.† The specific surface area was about 15.179 m^2 g^{-1}, and the main pore size was about 3.063 nm in diameter. To verify the content of the prepared sample, ICP-AES was used to determine the contents of Mo and Ti. The Mo and Ti contents in TiO_2@G@MoS_2@C were found to be 29.66% and 0.43%, respectively. The MoS_2 and TiO_2 contents were calculated to be 49.5% and 0.72%, respectively. The sulfur and carbon contents were analyzed by TGA. As shown in Fig. S2,† the weight loss occurring between 298 and 451 °C was mainly due to the oxidation of MoS_2 to MoO_3 and the removal of carbon. The remaining product after 500 °C was pure MoO_3 with the weight percentage of 46.7%. The content of MoS_2 was calculated to be 51.9%, which was approximately consistent with the ICP-AES result.

Fig. 7a shows the CV curves of carbon-coated TiO_2@G@MoS_2 electrode compared with those of the uncoated sample. The carbon-coated core–shell TiO_2@G@MoS_2 electrode had a lower anodic peak potential (2.31 V) and a higher cathodic peak potential (0.56 V), suggesting its better electrochemical reactivity and reversibility. The charge–discharge voltage profiles were obtained at the current density of 0.1 A g^{-1}, indicating initial discharge and charge capacities of 1208 and 933 mA h g^{-1}, respectively, and the coulombic efficiency of 76.6% (Fig. 7b).

Fig. 7c shows the cycling performance of the carbon-coated TiO_2@G@MoS_2 hollow spheres at the current density of 0.1 A g^{-1} between 0.01 and 3.0 V. It exhibits enhanced capacity retention stability and high reversible capacity of 823 mA h g^{-1} even after 100 cycles, which is 88% of the capacity retention of the initial charge capacity. Moreover, the coulombic efficiency quickly stabilized at around 99% from the 4th cycle and was maintained in the following cycles. Compared to other TiO_2/MoS_2 composites, the carbon-coated TiO_2@G@MoS_2 hollow spheres showed higher electrochemical energy storage

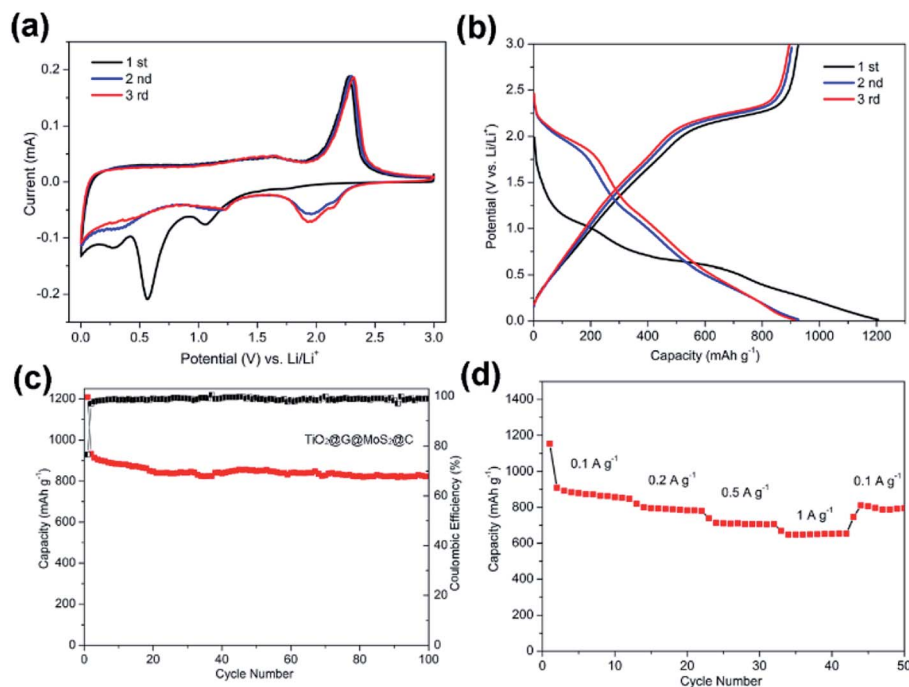**Fig. 7** (a) Cyclic voltammetry curves of the $TiO_2@G@MoS_2@C$ hollow nanospheres at the scan rate of 0.5 mV s^{-1} in the voltage range of 0.01–3 V (*vs.* Li/Li$^+$). (b) Charge–discharge voltage profiles at the 1st, 2nd and 3rd cycle at the current density of 0.1 A g^{-1} of the $TiO_2@G@MoS_2@C$ hollow nanospheres. (c) Cycling performance of $TiO_2@G@MoS_2@C$ hollow sphere electrodes, and corresponding coulombic efficiency. (d) Rate capability of the $TiO_2@G@MoS_2@C$ electrode.

performances,[17–25] especially high reversible capacity, which was attributed to the synergistic effects of all the components. The rate performance test was carried out for the carbon-coated $TiO_2@G@MoS_2$ hollow spheres to investigate their stability. The specific capacities of the composite were 850, 783, 700 and 650 mA h g^{-1} upon cycling at 0.1, 0.2, 0.5 and 1 A g^{-1}, respectively. When the current density was reset to 0.1 A g^{-1}, the capacity could still return to 850 mA h g^{-1}; this confirmed the outstanding rate capability. We carried out the SEM and TEM characterization for the as-prepared electrodes of $TiO_2@$-$G@MoS_2@C$ and $TiO_2@G@MoS_2$ hollow spheres after cycling. As shown in Fig. S3,† the SEI films of the $TiO_2@G@MoS_2$ electrode were clearly thicker than those of the carbon-coated electrode (Fig. S3c and d†). Fig. S4† exhibits the TEM image of the as-prepared electrodes; the carbon hollow nanostructure was well preserved after 50 cycles, whereas the MoS_2 particle was not observed on the carbon sphere surface for the $TiO_2@$-$G@MoS_2$ hollow spheres sample; this was due to the detachment and diffusion of MoS_2. Fig. S4c and d† show the TEM images of $TiO_2@G@MoS_2@C$, in which the hollow structure is well maintained, and the MoS_2 particles distributed in the carbon coating shells can be still seen; this indicates the superior structural stability of $TiO_2@G@MoS_2@C$ during long-term cycling.

The excellent cycling stability and remarkable rate capability of the hierarchical multiple-layer carbon-coated $TiO_2@$-$G@MoS_2$ hollow spheres could be attributed to their unique structural advantages and synergistic effect. First, the graphitic carbon-coated mesoporous TiO_2 hollow structure could

effectively buffer the mechanical strain accompanying the lithium intercalation/exfoliation, alleviate huge volume variation of MoS_2, and enhance the internal electronic conductivity of the hierarchical electrode.[63] Second, the vertically oriented MoS_2 laminated layers with high surface area provided a large electrode/electrolyte interface and shortened the diffusion paths for Li$^+$ ions, thus improving the dynamic performance of Li$^+$ storage.[64,65] Third, the carbon-coated top layer prevented MoS_2 from aggregation and pulverization, enhancing the electronic conductivity and contributing to the obvious improvement of long-term cycling stability.[66,67] Based on the synergistic effect of all the aforementioned merits, the rationally designed carbon-coated $TiO_2@G@MoS_2$ core–shell hollow sphere exhibited remarkable electrochemical performance for lithium-ion storage.

Experimental

Synthesis of carbon-coated $TiO_2@G@MoS_2$ hollow nanospheres

Colloidal SiO_2 nanospheres with a uniform diameter of 300 nm were fabricated by the Stöber method. For TiO_2 coating, 0.2 g of the as-obtained SiO_2 nanospheres was homogeneously dispersed in ethanol (150 mL). After this, ammonia solution (0.7 mL) was added to the suspension, and the mixture was stirred by a magnetic bar for 1 h. Then, tetrabutoxide titanate (TBOT, 2.0 mL) was added, and the reaction was proceeded at 45 °C for 24 h under continuous stirring. To produce the graphitic carbon-coated $SiO_2@TiO_2$ spheres, the $SiO_2@TiO_2$ core–shell

structured spheres were homogeneously dispersed in a glucose solution (0.1 M, 15 mL) and hydrothermally treated at 180 °C for 2 h; this yielded the $SiO_2@TiO_2@C$ spheres. Then, the amorphous TiO_2/C shells could be converted to crystalline TiO_2/graphitic carbon hybrid structures after annealing at 800 °C.

To grow the hierarchical MoS_2 shell on the graphitic carbon intermediate layer, 0.2 g of $SiO_2@TiO_2@G$ sphere templates were dispersed in 60 mL of de-ionized water and 20 mL ethanol solution. Then, 0.6 g of sodium molybdate ($Na_2MoO_4\cdot2H_2O$) and 2.5 g of L-cysteine were added to the abovementioned solution. After ultrasonication, the reaction solution was then transferred to a Teflon-lined stainless steel autoclave and hydrothermally treated at 180 °C for 24 h. After etching of SiO_2 by a 5% HF solution, 0.08 g of the as-obtained hollow nanospheres were dispersed in 2.82 mL of ethanol and 7.04 mL of deionized water, followed by the addition of 0.23 g cetyltrimethylammonium bromide (CTAB), 0.035 g resorcinol and 0.01 mL ammonia. After stirring at 35 °C for 30 min, 0.05 mL formalin was added to the dispersion. Then, the reaction was proceeded at 35 °C for 6 h under continuous stirring. The obtained polymer-coated $TiO_2@G@MoS_2$ was annealed at 600 °C for 2 h under a high vacuum atmosphere, and then, the carbon-coated $TiO_2@G@MoS_2$ hollow nanospheres were obtained.

Material characterization

The morphology information was determined by the FEI Sirion 200 scanning electron microscope (SEM) and the JEOL 2100F transmission electron microscope (TEM). Samples were characterized by X-ray diffraction (XRD, Rigaku Ultima IV X-ray Diffractometer) equipped with Cu Kα radiation. Surface composition of the sample was analyzed by X-ray photoelectron spectroscopy (XPS, AXIS ULTRA DLD, Kratos, Japan). Raman spectroscopy was conducted using the Renishaw inVia-reflex system at room temperature. A laser with the wavelength of 532 nm was used as the excitation source. Inductively coupled plasma-atomic emission spectrometry (ICP-AES, Thermo, iCAP7600) was used for detecting the concentrations of Mo and Ti ions. Thermogravimetric analysis (TGA) was carried out using a thermogravimetric analysis instrument (TGA, SDT Q600 V8.2 Build 100).

Electrochemical measurements

The electrochemical tests were carried out in coin cells. The working electrode consisted of 80 wt% of active material, 10 wt% of conductive carbon black, and 10 wt% of polymer binder (polyvinylidene fluoride, PVDF). The electrolyte was 1 M $LiPF_6$ in a mixture of ethylene carbonate (EC), dimethyl carbonate (DMC) and diethyl carbonate (DEC) (1 : 1 : 1 by volume). The typical mass loading of the active materials was about 1 mg cm^{-2}. Lithium disc was used as both the counter electrode and the reference electrode. Cell assembly was carried out in an Ar-filled glove box with moisture and oxygen concentrations below 1.0 ppm. The charge–discharge tests were performed using the Land CT2001A battery test system. Cyclic voltammograms (CVs) were obtained using the CHI 660D electrochemical workstation.

Conclusions

In summary, a hybrid architecture of carbon-coated $TiO_2@$-$G@MoS_2$ has been successfully synthesized. The hierarchical MoS_2 hollow spheres with high theoretical capacity were sandwiched by graphite and microporous carbon. The role of the carbon layer in the electrochemical energy storage performance was systematically investigated, and the key factors that controlled the capacity and cycling stability were identified. Due to the unique hierarchical core–shell nanostructure and the synergistic effect of every component, the rationally designed carbon-coated $TiO_2@G@MoS_2$ hollow sphere electrode exhibited high charge capacity and the cycling stability of 823 mA h g^{-1} at the current density of 100 mA g^{-1} after 100 cycles, retaining almost 88% of the initial reversible capacity with the high coulombic efficiency of 99%. Our study suggests a new mean for the synthesis of high-performance core/shell structure electrodes by the introduction of a carbon shell or interlayer for energy storage, which is expected to be widely extended to metal oxides or metal sulfides.

Conflicts of interest

There are no conflicts to declare.

Acknowledgements

References

1 V. Etacheri, R. Marom, R. Elazari, G. Salitra and D. Aurbach, *Energy Environ. Sci.*, 2011, **4**, 3243.

2 F. Cheng, J. Liang, Z. Tao and J. Chen, *Adv. Mater.*, 2011, **23**, 1695.

3 B. Dunn and J. M. Tarascon, *Science*, 2011, **334**, 928.

4 M. Armand and J. M. Tarascon, *Nature*, 2008, **451**, 652.

5 J. B. Goodenough and K. S. Park, *J. Am. Chem. Soc.*, 2013, **135**, 1167.

6 J. Liu and X. W. Liu, *Adv. Mater.*, 2012, **24**, 4097.

7 M.-R. Gao, Y.-F. Xu, J. Jiang and S.-H. Yu, *Chem. Soc. Rev.*, 2013, **42**, 2986.

8 P. Poizot, S. Laruelle, S. Grugeon, L. Dupont and J. M. Tarascon, *Nature*, 2000, **407**, 496.

9 M. Chhowalla, H. S. Shin, G. Eda, L. J. Li, K. P. Loh and H. Zhang, *Nat. Chem.*, 2013, **5**, 263.

10 X. Huang, Z. Zeng and H. Zhang, *Chem. Soc. Rev.*, 2013, **42**, 1934.

11 H. Hwang, H. Kim and J. Cho, *Nano Lett.*, 2011, **11**, 4826.

12 J. Z. Wang, L. Lu, M. Lotya, J. N. Coleman, S. L. Chou, H. K. Liu, A. I. Minett and J. Chen, *Adv. Energy Mater.*, 2013, **3**, 798.

13 C. Zhang, Z. Wang, Z. Guo and X. W. Lou, *ACS Appl. Mater. Interfaces*, 2012, **4**, 3765.

14 F. Xiong, Z. Cai, L. Qu, P. Zhang, Z. Yuan, O. K. Asare, W. Xu, C. Lin and L. Mai, *ACS Appl. Mater. Interfaces*, 2015, 7, 12625.

15 X. Zhou, L. J. Wan and Y. G. Guo, *Nanoscale*, 2012, **4**, 5868.

16 L. Hu, Y. Ren, H. Yang and Q. Xu, *ACS Appl. Mater. Interfaces*, 2014, **6**, 14644.

17 R. Dai, A. Zhang, Z. Pan, A. M. Alenizi, A. A. Elzatahry, L. Hu and G. Zheng, *Small*, 2016, **12**, 2792.

18 B. Chen, N. Zhao, L. Guo, F. He, C. Shi, C. He, J. Li and E. Liu, *Nanoscale*, 2015, **7**, 12895.

19 X. Xu, Z. Fan, S. Ding, D. Yu and Y. Du, *Nanoscale*, 2014, **6**, 5245.

20 X. Li, W. Li, M. Li, P. Cui, D. Chen, T. Gengenbach, L. Chu, H. Liu and G. Song, *J. Mater. Chem.*, 2014, **3**, 2762.

21 X. Zhu, C. Yang, F. Xiao, J. Wang and X. Su, *New J. Chem.*, 2014, **39**, 683.

22 M. Mao, L. Mei, D. Guo, L. Wu, D. Zhang, Q. Li and T. Wang, *Nanoscale*, 2014, **6**, 12350.

23 B. Guo, K. Yu, H. Fu, Q. Hua, R. Qi, H. Li, H. Song, S. Guo and Z. Zhu, *J. Mater. Chem. A*, 2015, **3**, 6392.

24 B. Chen, E. Liu, F. He, C. Shi, C. He, J. Li and N. Zhao, *Nano Energy*, 2016, **26**, 541.

25 J. Y. Liao, B. D. Luna and A. Manthiram, *J. Mater. Chem. A*, 2015, **4**, 801.

26 M. Wagemaker, G. J. Kearley, A. A. van Well, H. Mutka and F. M. Mulder, *J. Am. Chem. Soc.*, 2003, **125**, 840.

27 C. Luo, Y. Xu, Y. Zhu, Y. Liu, S. Zheng, A. Langrock and C. Wang, *ACS Nano*, 2013, **7**, 8003.

28 J. Liu, P. Kopold, C. Wu, P. A. V. Aken, J. Maier and Y. Yu, *Energy Environ. Sci.*, 2015, **8**, 3531.

29 K. Chang and W. Chen, *ACS Nano*, 2011, **5**, 4720.

30 J. Xiao, X. Wang, X. Q. Yang, S. Xun, G. Liu, P. K. Koech, J. Liu and J. P. Lemmon, *Adv. Funct. Mater.*, 2011, **21**, 2840.

31 S. H. Choi, Y. N. Ko, J.-K. Lee and Y. C. Kang, *Adv. Funct. Mater.*, 2015, **25**, 1780.

32 K. Chang, D. Geng, X. Li, J. Yang, Y. Tang, M. Cai, R. Li and X. Sun, *Adv. Energy Mater.*, 2013, **3**, 839.

33 X. Cao, Y. Shi, W. Shi, X. Rui, Q. Yan, J. Kong and H. Zhang, *Small*, 2013, **9**, 3433.

34 X. Xie, Z. Ao, D. Su, J. Zhang and G. Wang, *Adv. Funct. Mater.*, 2015, **25**, 1393.

35 X.-Y. Yu, H. Hu, Y. Wang, H. Chen and X. W. Lou, *Angew. Chem., Int. Ed.*, 2015, **127**, 7503.

36 X. Li, J. Zhang, R. Wang, H. Huang, C. Xie, Z. Li, J. Li and C. Niu, *Nano Lett.*, 2015, **15**, 5268.

37 Y. Shi, Y. Wang, J. I. Wong, A. Y. S. Tan, C.-L. Hsu, L.-J. Li, Y.-C. Lu and H. Y. Yang, *Sci. Rep.*, 2013, **3**, 2169.

38 S. Ding, J. S. Chen and X. W. Lou, *Chem.–Eur. J.*, 2011, **17**, 13142.

39 Y. Fang, Y. Lv, F. Gong, A. A. Elzatahry, G. Zheng and D. Zhao, *Adv. Mater.*, 2016, **28**, 9385.

40 J. Wang, C. Luo, T. Gao, A. Langrock, A. C. Mignerey and C. Wang, *Small*, 2015, **11**, 473.

41 K. Chang, W. Chen, L. Ma, H. Li, H. Li, F. Huang, Z. Xu, Q. Zhang and J.-Y. Lee, *J. Mater. Chem.*, 2011, **21**, 6251.

42 C. Zhu, X. Mu, P. A. van Aken, Y. Yu and J. Maier, *Angew. Chem., Int. Ed.*, 2014, **53**, 2152.

43 H. Jiang, D. Ren, H. Wang, Y. Hu, S. Guo, H. Yuan, P. Hu, L. Zhang and C. Li, *Adv. Mater.*, 2015, **27**, 3687.

44 J. Zhou, J. Qin, X. Zhang, C. Shi, E. Liu, J. Li, N. Zhao and C. He, *ACS Nano*, 2015, **9**, 3837.

45 B. Jiang, C. Han, B. Li, Y. He and Z. Lin, *ACS Nano*, 2016, **10**, 2728–2735.

46 B. Jiang, Y. He, B. Li, S. Zhao, S. Wang, Y.-B. He and Z. Lin, *Angew. Chem., Int. Ed.*, 2017, **56**, 1869–1872.

47 W. Stöber, A. Fink and E. Bohn, *J. Colloid Interface Sci.*, 1968, **26**, 62.

48 S. Liang, J. Zhou, J. Liu, A. Pan, Y. Tang, T. Chen and G. Fang, *CrystEngComm*, 2013, **15**, 4998.

49 H. Liu, D. Su, R. Zhou, B. Sun, G. Wang and S. Z. Qiao, *Adv. Energy Mater.*, 2012, **2**, 970.

50 X. Chen, L. Liu, P. Y. Yu and S. S. Mao, *Science*, 2011, **331**, 746.

51 A. C. Ferrari and J. Robertson, *Phys. Rev. B: Condens. Matter Mater. Phys.*, 2008, **61**, 14095.

52 K. K. Liu, W. Zhang, Y. H. Lee, Y. C. Lin, M. T. Chang, C. Y. Su, C. S. Chang, H. Li, Y. Shi and H. Zhang, *Nano Lett.*, 2012, **12**, 1538.

53 Y. H. Chang, C. T. Lin, T. Y. Chen, C. L. Hsu, Y. H. Lee, W. Zhang, K. H. Wei and L. J. Li, *Adv. Mater.*, 2013, **25**, 756.

54 T. Stephenson, Z. Li, B. Olsen and D. Mitlin, *Energy Environ. Sci.*, 2014, **7**, 209.

55 M. Lin, J. Ye, W. Chen, D. Chen and J. Y. Lee, *Nano Energy*, 2014, **10**, 144.

56 X. Fang, X. Yu, S. Liao, Y. Shi, Y. S. Hu, Z. Wang, G. D. Stucky and L. Chen, *Microporous Mesoporous Mater.*, 2012, **151**, 418.

57 M. Mao, L. Mei, D. Guo, L. Wu, D. Zhang, Q. Li and T. Wang, *Nanoscale*, 2014, **6**, 12350.

58 X. Jiang, X. Yang, Y. Zhu, H. Jiang, Y. Yao, P. Zhao and C. Li, *J. Mater. Chem. A*, 2014, **2**, 11124.

59 Y. Sun, J. Zhu, L. Bai, Q. Li, X. Zhang, W. Tong and Y. Xie, *Inorg. Chem. Front.*, 2014, **1**, 58.

60 X. Wang, Z. Zhang, Y. Chen, Y. Qu, Y. Lai and J. Li, *J. Alloys Compd.*, 2014, **600**, 84.

61 S. Ding, D. Zhang, J. S. Chen and X. W. Lou, *Nanoscale*, 2012, **4**, 95.

62 Z. Cai, L. Xu, M. Yan, C. Han, L. He, K. M. Hercule, C. Niu, Z. Yuan, W. Xu, L. Qu, K. Zhao and L. Mai, *Nano Lett.*, 2015, **15**, 738.

63 S. Zhao, Z. Wang, Y. He, B. Jiang, Y. Harn, X. Liu, F. Yu, F. Feng, Q. Shen and Z. Lin, *ACS Energy Lett.*, 2017, **2**, 111–116.

64 L. Zhang, H. B. Wu, Y. Yan, X. Wang and X. W. Lou, *Energy Environ. Sci.*, 2014, **7**, 3302.

65 L. Zhang and X. W. Lou, *Chem.–Eur. J.*, 2014, **20**, 5219.

66 A. P. Tiwari, H. Yoo, J. Lee, D. Kim, J. H. Park and H. Lee, *Nanoscale*, 2015, **7**, 11928.

67 D. Xie, X. Xia, Y. Zhong, Y. Wang, D. Wang, X. Wang and J. Tu, *Adv. Energy Mater.*, 2017, **7**, 1601804.